J. Phys.: Condens. Matter **25** (2013) 416001 (15pp) doi:10.1088/0953-8984/25/41/416001

Paramagnetism and antiferromagnetic interactions in single-phase Fe-implanted ZnO

L M C Pereira[1,2,3], U Wahl[3], J G Correia[3], M J Van Bael[4], K Temst[1], A Vantomme[1] and J P Araújo[2]

[1] Instituut voor Kern- en Stralingsfysica, KU Leuven, B-3001 Leuven, Belgium
[2] IFIMUP and IN-Institute of Nanoscience and Nanotechnology, Universidade do Porto, 4169-007 Porto, Portugal
[3] Instituto Tecnológico e Nuclear, Instituto Superior Técnico, Universidade Técnica de Lisboa, 2686-953 Sacavém, Portugal
[4] Laboratory of Solid-State Physics and Magnetism, KU Leuven, B-3001 Leuven, Belgium

E-mail: lino.pereira@fys.kuleuven.be

Received 4 July 2013, in final form 9 August 2013
Published 11 September 2013
Online at stacks.iop.org/JPhysCM/25/416001

Abstract
As the intrinsic origin of the high-temperature ferromagnetism often observed in wide-gap dilute magnetic semiconductors becomes increasingly debated, there is a growing need for comprehensive studies on the single-phase region of the phase diagram of these materials. Here we report on the magnetic and structural properties of Fe-doped ZnO prepared by ion implantation of ZnO single crystals. A detailed structural characterization shows that the Fe impurities substitute for Zn in ZnO in a wurtzite $Zn_{1-x}Fe_xO$ phase which is coherent with the ZnO host. In addition, the density of beam-induced defects is progressively decreased by thermal annealing up to 900 °C, from highly disordered after implantation to highly crystalline upon subsequent annealing. Based on a detailed analysis of the magnetometry data, we demonstrate that *isolated* Fe impurities occupying Zn-substitutional sites behave as localized paramagnetic moments down to 2 K, irrespective of the Fe concentration and the density of beam-induced defects. With increasing local concentration of Zn-substitutional Fe, strong nearest-cation-neighbor antiferromagnetic interactions favor the antiparallel alignment of the Fe moments.

(Some figures may appear in colour only in the online journal)

1. Introduction

The current view on wide-gap dilute magnetic semiconductors (DMS) is moving towards the belief that the often observed high-temperature ferromagnetism is not intrinsic, i.e. that it does not result from long-range magnetic order of randomly distributed magnetic dopants [1]. While limited experimental evidence exists that some DMS materials are intrinsically ferromagnetic at room temperature, a number of non-intrinsic sources of ferromagnetic-like behavior have been identified and are becoming increasingly well documented: magnetic contamination [2–5], instrumental artifacts [4–6] and chemical and/or structural segregation of the transition metal dopants into non-DMS phases [7–17].

Following the first report of high-temperature ferromagnetism in Co-doped TiO_2 [18] and the prediction by Dietl *et al* [19] that highly p-type Mn-doped ZnO and GaN could attain a Curie temperature (T_C) above room temperature, ferromagnetism at and above room temperature has been reported in a rapidly growing number of wide-gap DMS materials (cf e.g. the reviews [20–23]). However, with the growing understanding of the most studied of these materials, issues of irreproducibility and instability became increasingly evident. Reports began to emerge which

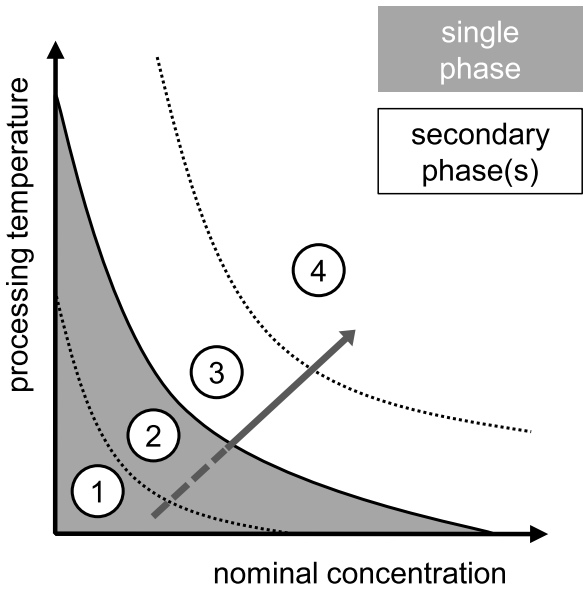

Figure 1. Representation of the structural phase diagram of a DMS system (described in detail in the text).

comprehensively described the magnetic behavior of some of these materials (e.g. [24–30]). Doing so requires covering growth, doping and post-processing conditions within relevant ranges, and performing both (1) magnetic characterization which carefully takes into account potential magnetic contamination and technique-specific artifacts, and (2) structural characterization which undeniably establishes either the single-phase character of the DMS material or identifies the segregated secondary phases. Such combined magneto-structural characterization, which typically implies using other than standard lab equipment (cf for example [30, 17]), then allows one to position a given DMS sample (in a given processing step) within the system's phase diagram.

Figure 1 illustrates the generic *structural* phase diagram for a DMS system consisting of a semiconductor (A_yB_z) doped with a transition metal (X). The main coordinates in such a diagram are the processing temperature (of growth, implantation or annealing) and the nominal concentration (x) of the transition metal dopant, although the preparation method may also play an important role. The gray area represents the single-phase region, where the transition metal impurities substitute one of the host constituents (e.g. element A), maintaining the host's crystal structure by forming a $A_{y-x}X_xB_z$ alloy. The impurities may be randomly distributed (region (1)) or, for a sufficiently high concentration or temperature, aggregate in impurity-rich regions; i.e. x may vary across the $A_{y-x}X_xB_z$ alloy without a well-defined interface (region (2)). For a sufficiently high processing temperature or concentration (white region), the transition metal impurities may segregate into small precipitates of a $A_{y'}X_{x'}B_{z'}$ (where y' and/or z' can be 0) secondary phase with a different structure from that of the host. Depending on various factors, such as processing temperature, impurity concentration and preparation method, different secondary phases may form (regions (3) and (4)).

The *magnetic* phase diagram of a DMS system can be pictured as an over-layer of the structural phase diagram of figure 1. In the true DMS region of the phase diagram (region (1)), the transition metal impurities are randomly and substitutionally distributed in the host. *Intrinsic ferromagnetism* can be defined as ferromagnetic order of the localized moments of these randomly distributed transition metal impurities via a long-range order mechanism, as is the case in *narrow-gap* DMS such as $Ga_{1-x}Mn_xAs$ and $In_{1-x}Mn_xAs$ [1]. However, comprehensive studies on this region of the phase diagram of *wide-gap* DMS systems, on carefully characterized single-phase materials, revealed only paramagnetism (e.g. in Co-doped ZnO [25] and Mn-doped GaN [24]), antiferromagnetic interactions (e.g. in Co-doped ZnO [27, 28, 31, 32], Mn-doped GaN [26, 33], and Cr in GaN [34]), or at best, ferromagnetic order with a very low T_C (e.g. $T_C < 10$ K in Mn-doped GaN [35]). With increasing processing temperature (either during growth, implantation or annealing), the impurities tend to aggregate and segregate. This segregation may be only chemical (region (2)), i.e. the crystal structure is maintained and only the local impurity concentration varies across the material, alternating between impurity-rich and impurity-poor regions (e.g. in Co-doped ZnO [7] and Mn-doped GaN [8]). For sufficiently high concentration and temperature, phase segregation may occur (regions (3) and (4)), i.e. the impurities precipitate in nanocomposites with a well-defined interface with the host structure (e.g. in ZnO doped with Fe, Co and Ni [9–17]).

Fe-implanted ZnO is a rich DMS system in which to explore the different regions of such a complex magneto-structural phase diagram. The fact that the Fe impurities are incorporated by ion implantation offers the potential advantage that ion bombardment results in lattice disorder, which in turn has been proposed to promote ferromagnetic order of magnetic impurities in single-phase DMS materials, either in the form of point defects in bound magnetic polaron (BMP) models [36], or in the form of extended defects in charge transfer ferromagnetism (CTF) models [37]. In addition, Fe impurities may be incorporated in ZnO both as Fe^{2+} and Fe^{3+}, making it a potentially suitable mixed-valency impurity in CTF systems. However, despite the various reports of intrinsic ferromagnetism in Fe-implanted ZnO (e.g. [38–41]), the extensive work by Zhou *et al* on carefully characterized samples has shown that the ferromagnetic-like behavior originates from superparamagnetic precipitates formed at sufficiently high processing temperatures and Fe concentrations: α-Fe clusters (region (3) in figure 1) which are oxidized and then converted to the spinel ferrite $ZnFe_2O_4$ (region (4) in figure 1) with increasing annealing temperature and duration [9–12]. Although this segregated region of the phase diagram of Fe-implanted ZnO is rather well established (continuous part of the arrow in figure 1), both in terms of structure and magnetism, the magnetic behavior of the Fe impurities in single-phase $Zn_{1-x}Fe_xO$ is still poorly understood (dashed part of the arrow in figure 1, i.e. regions (1) and (2)).

In this paper, we investigate the magnetism of single-phase $Zn_{1-x}Fe_xO$ prepared by Fe^+ ion implantation in ZnO

single crystals. By varying the nominal Fe concentration and the degree of structural disorder, we aim at identifying the type of magnetic interactions between the Fe moments and how it is affected by implantation-induced disorder.

2. Experimental details

Commercial ZnO wurtzite [0001] single crystals (CrysTec GmbH), hydrothermally grown, were implanted with $^{56}Fe^{+}$ ions at room temperature to three different fluences: 1×10^{15}, 5×10^{15} and 1×10^{16} at. cm^{-2}, referred to below as S1, S5 and S10 respectively. An implantation energy of 60 keV and a beam angle of 10° with respect to the sample surface (to minimize ion channeling) results in a peak atomic concentration x_p of 0.0068 (0.68%), 0.034 (3.4%) and 0.068 (6.8%), at a projected ion range R_p of 297 Å (mean depth) with a straggling of 134 Å (square root of the variance), estimated using MARLOWE [42]. In order to avoid sample contamination with ferromagnetic material [2], the implantations were carried out using a Mo sample-holder and the samples were placed in a ceramic boat during annealing. Three samples were prepared for each of the fluences: one for magnetic characterization using SQUID magnetometry, one for damage characterization using Rutherford backscattering and channeling spectrometry (RBS/C) and one for Fe lattice location using β^- emission channeling. Structural and magnetic characterization were performed in the as-implanted samples and after thermal annealing in vacuum ($<10^{-5}$ mbar) in 100 °C steps (10 min each step) up to 900 °C.

2.1. SQUID magnetometry

The magnetic characterization was performed using a superconducting quantum interference device (SQUID) magnetometer (*Quantum Design* MPMS XL-5) following strict procedures in order to avoid measurement artifacts and external magnetic contributions. These procedures were developed based on statistically relevant tests, which allowed us to determine the practical limits of SQUID magnetometry for the detection of ferromagnetism under various sample preparation, processing and handling conditions [2]. All measurements were performed with the field perpendicular to the *c*-axis, i.e. , parallel to the sample plane.

2.2. Rutherford backscattering and channeling spectrometry (RBS/C)

Defect accumulation and recovery were characterized using Rutherford backscattering and channeling spectrometry (RBS/C), with a 1.57 MeV He^{+} beam and two detectors at backscattering angles of 168° and 105°. The 168° backscattering geometry was used to characterize the channeling minimum yield χ_{min} along the [0001] axis. χ_{min} is the ratio of the backscattering yield with the incident beam aligned with the crystal axis to the yield for a random beam incidence, and is a measure of the lattice disorder induced by ion implantation [43]. The 15° glancing exit angle geometry (with respect to the sample surface) of the second detector was used to obtain enhanced depth resolution of the damage profile.

2.3. β^- emission channeling

The emission channeling (EC) technique allows one to determine the lattice location of impurities in single crystals, making use of the charged particles emitted by a radioactive isotope of the impurity element under study [44]. The screened Coulomb potential of atomic rows and planes determines the anisotropic scattering of the particles emitted isotropically during decay. Along low-index crystal directions of single crystals, this anisotropic scattering results in well-defined channeling or blocking effects. Because these effects strongly depend on the initial position of the emitted particles, they result in emission patterns which are characteristic of the lattice site(s) occupied by the probe atoms. Several reviews on emission channeling can be found in the literature [44–47], and the technique has previously been used to investigate the lattice location of Fe [48], Co [49], Mn [49], and Cu [50] in ZnO, in the low fluence ($\sim 10^{13}$ cm^{-2}) regime.

Each of the three samples implanted with stable ^{56}Fe for emission channeling experiments, were subsequently co-implanted with radioactive ^{59}Fe (with a half-life $t_{1/2} = 46$ d) up to a fluence of 2×10^{13} cm^{-2}, by implanting the precursor isotope ^{59}Mn ($t_{1/2} = 4.6$ s) which decays to ^{59}Fe. The radioactive implantations were carried out at the on-line isotope separator facility ISOLDE at CERN, which provides mass-separated beams of radioactive Mn isotopes produced by means of 1.4-GeV proton-induced nuclear fission from uranium carbide UC_2 targets and chemically selective laser ion sources [51]. The β^- decay of ^{59}Mn transfers a recoil energy of about 200 eV to its ^{59}Fe daughter. This ensures that the ^{59}Fe atoms are re-implanted, i.e. that they do not inherit the ^{59}Mn lattice site. The implantations were performed at room temperature, under a tilt angle of 7° with respect to the surface normal, with an energy of 60 keV, resulting in a projected range R_P of 299 Å and a 136 Å straggling, estimated using the MARLOWE code [42]. Since the concentration of radioactive ^{59}Fe probes is at least two orders of magnitude below that of stable ^{56}Fe, the increase in total Fe concentration compared to the samples used for RBS/C and SQUID measurements can be neglected. In addition, because the depth profiles of ^{56}Fe and ^{59}Fe overlap almost perfectly (R_p is 297 and 299 Å and straggling is 134 and 136 Å for ^{56}Fe and ^{59}Fe, respectively), one can assume that the ^{59}Fe probes accurately represent the site location behavior of all Fe impurities.

Angular-dependent emission yields of the β^- particles emitted during decay were measured at room temperature, along four crystallographic directions ([0001], [$\bar{1}$102], [$\bar{1}$101] and [$\bar{2}$113]), in the as-implanted state and after *in situ* capless annealing in vacuum ($<10^{-5}$ mbar) up to 900 °C. These patterns were recorded using a position- and energy-sensitive detection system similar to that described in [52]. Using the *many-beam* formalism for electron channeling in single crystals [44], theoretical emission patterns were calculated for probes occupying substitutional Zn (S_{Zn}) and O (S_O) sites with varying root-mean-square (rms) displacements, the main interstitial sites and interstitial sites resulting from

displacements along the [0001] or the basal directions. Quantitative lattice location is provided by fitting the experimental patterns with theoretical ones using the two-dimensional fit procedure outlined in [52]. Corrections for secondary electrons that reach the detector were implemented by subtracting an isotropic background from every pattern. This secondary electron contribution was estimated based on Geant4 [53, 54] simulations of electron scattering, taking into account the elemental composition and geometry of the sample, sample-holder and vacuum chamber.

3. Results and analysis

Since the first question to address concerns the existence of room-temperature ferromagnetism, we start by discussing the SQUID magnetometry data at room temperature. This then sets the direction of the discussion in terms of structure (impurity lattice location and structural disorder) and a more detailed analysis of the magnetic behavior based on low-temperature SQUID magnetometry.

3.1. SQUID magnetometry at room temperature

For all samples, following some of the annealing steps, a small hysteresis could be resolved in the 300 K *M–H* data (magnetic moment μ as a function of applied field H) after subtracting the substrate's diamagnetic background (figures 2(a) and (b)). Figure 2(c) compiles the saturation moment μ_{sat} of this residual ferromagnetic component, for the three fluences, as a function of annealing temperature. The saturation moment remains consistently below 5×10^{-7} emu and appears to increase with annealing temperature. We attribute this residual ferromagnetism to sample contamination, since there is no correlation with implanted fluence and since the same type of residual hystereses are observed in unimplanted control samples [2]. The apparent increase in saturation moment with annealing temperature (figure 2) is simply a consequence of the increase in number of processing steps, i.e. an increasing number of potentially contaminating events. In any case, one cannot exclude that some residual ferromagnetic moment arises from intrinsic ferromagnetism associated with the Fe doping or other beam-induced defects such as vacancies or self-interstitials. Based on the maximum saturation value for each fluence, table 1 lists the maximum ferromagnetic moment per Fe atom, assuming that all Fe atoms equally contribute to the ferromagnetic component. Ferromagnetic-like behavior can also be observed if a fraction of the implanted Fe precipitates in superparamagnetic α-Fe clusters, as demonstrated by Zhou *et al* [9–12]. Table 1 also lists the maximum fraction of precipitated Fe, assuming that all the ferromagnetic-like moment originates from α-Fe clusters with a moment per Fe atom of 2.2 μ_B (of bulk α-Fe). Note that the higher fraction for the lower fluence sample is merely a consequence of dividing a similar saturation moment by a much smaller number of atoms. Since the fraction of Fe atoms in clusters is expected to increase with Fe concentration [11], one can conclude that the maximum fraction of clustered Fe in our samples is given by the value obtained for the highest fluence, i.e. less than 1%.

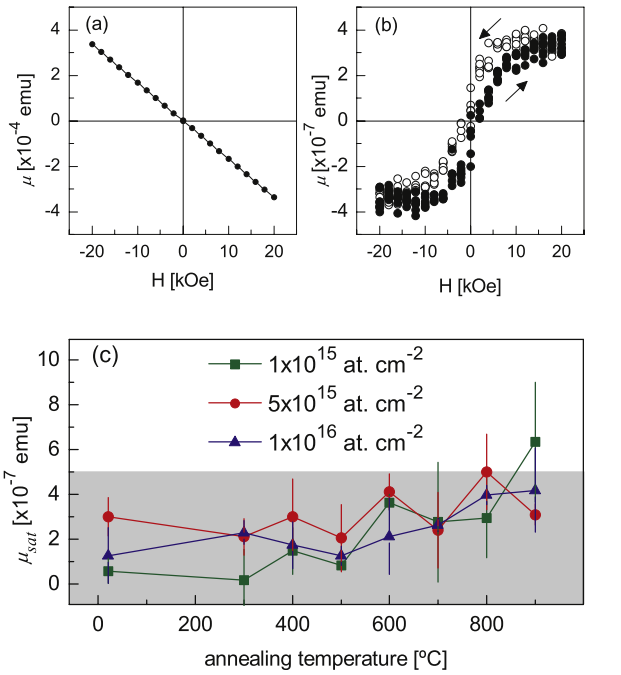

Figure 2. (a) 300 K *M–H* data of sample S1 following 600 °C annealing. (b) Data after subtraction of the diamagnetic component estimated from the linear fit of the high-field (10–20 kOe) magnetization (arrows indicate increasing and decreasing field). (c) Saturation moment μ_{sat} for all three samples, as a function of annealing temperature, obtained from the linear fit to the 300 K *M–H* data. All three samples have an area of approximately 0.25 cm^2 and, therefore, the data can be compared directly. The shaded area below 5×10^{-7} emu corresponds to the typical magnitude of the signal resulting from ferromagnetic-like contamination and measurement artifacts, i.e. the reliability limit for the detection of ferromagnetism [2, 6].

Table 1. Comparison between the amount of Fe atoms in each sample and the ferromagnetic saturation moment of the 300 K *M–H* data: maximum moment per Fe atom (μ_{Fe}), assuming that all Fe atoms equally contribute to the ferromagnetic component; maximum fraction of Fe impurities in α-Fe precipitates, assuming a moment per Fe atom of 2.2 μ_B.

Sample	Fluence (at. cm^{-2})	max. μ_{Fe} (μ_B)	max. α-Fe fraction (%)
S1	1×10^{15}	0.18	8.1
S5	5×10^{15}	0.05	2.4
S10	1×10^{16}	0.02	0.8

3.2. Characterization of structural disorder using RBS/C

Figure 3(a) shows representative RBS/C spectra measured in a backscattering geometry (168°) for an unimplanted sample and sample S5 after different annealing steps. As typical for ZnO (e.g. [55]), lattice disorder in the Zn sublattice accumulates in two regions: (1) in the bulk of the crystal (bulk peak), where the energy loss is maximum as the implanted ions are slowed down to the point that nuclear stopping dominates over electronic stopping and the host atoms are thus more efficiently displaced; (2) near the sample surface (surface peak), which acts as a sink for mobile defects created

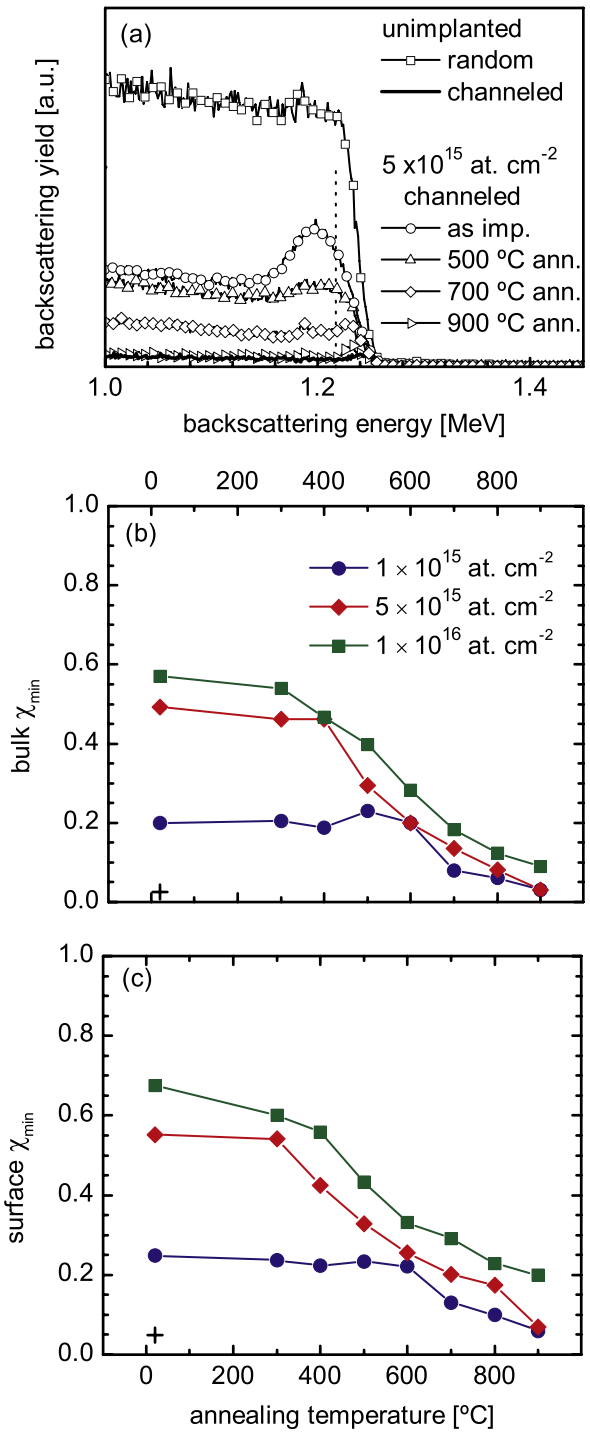

Figure 3. (a) RBS/C spectra measured in backscattering geometry (168°) aligned with the [0001] axis (channeling) for an unimplanted sample and sample S5 (5×10^{15} cm^{-2}) after different annealing steps, compared to the spectrum measured in a random beam orientation, for the unimplanted sample (the dashed line separates the surface and bulk energy windows used to calculate the corresponding χ_{min}). (b) Bulk and (c) surface χ_{min} of the three samples, as a function of annealing temperature. Bulk and surface χ_{min} of an unimplanted sample are also indicated (+).

during the ion bombardment. The channeling minimum yield χ_{min} is thus determined separately for these two regions. Bulk χ_{min} are plotted in figure 3(b) and surface χ_{min} in figure 3(c), for the three fluences and annealing steps up to 900 °C. High fluences (of the order of 1×10^{16} cm^{-2}) are required to induce significant lattice disorder ($\chi_{min} > 50$ %), which reflects the efficient *dynamic annealing* which characterizes ZnO and is responsible for its known high radiation resistance.

The beam-induced damage is removed quite efficiently by thermal annealing. Both bulk and surface χ_{min} decrease with increasing annealing temperature, particularly between 400 and 900 °C. After annealing at 900 °C, the bulk χ_{min} for fluences of 1×10^{15} and 5×10^{15} cm^{-2} (3% in both cases) are nearly the same as prior to implantation (2.5%). The recovery at the surface is also very efficient for these fluences, with χ_{min} of 6% and 7% for 1×10^{15} cm^{-2} and 5×10^{15} cm^{-2}, respectively, compared to 5% prior to implantation. For a fluence of 1×10^{16} cm^{-2} the recovery is somewhat less efficient, indicating that higher fluence implantation creates defect complexes which are more stable with respect to thermal annealing. This is in agreement with the general rule of thumb that annealing of extended defects in semiconductors requires a temperature of about two thirds of the material's melting point (in units of K) [56], which for ZnO corresponds to about 1200 °C. Nevertheless, a variation of the χ_{min} in the bulk region (i.e. in the region where the majority of the Fe impurities are located) from 67% in the as-implanted state down to 9% after 900 °C annealing is quite satisfactory for the purpose of this work. This brings up the question of how exactly the lattice recovery evolves with annealing within the bulk region. Figure 4 shows the RBS/C spectra measured in glancing geometry (which provides an increased depth resolution) of sample S10 after each annealing step. It shows that up to the 500 °C annealing step, the bulk peak does not decrease uniformly. Instead, the decrease in backscattering yield is less pronounced in the Fe end of range (EOR) region than in the region between the EOR and the surface, which results in an apparent shift of the bulk peak to the EOR. This indicates that the damage in the EOR region is more stable, being annealed only at 700 °C and above, which in turn suggests that the defects responsible for the increased backscattering yield in the bulk peak form complexes with the Fe impurities. This is discussed in more detail below, together with the emission channeling results on the lattice location of the Fe impurities.

As a final remark on figure 4, it is interesting to note that the low-temperature annealing (up to 500 °C) reveals an additional defect peak in the region between the surface and bulk defect peaks, which was also observed in Au-implanted ZnO [55] and coined as *middle defect peak* (MDP). In [55], the MDP was attributed to a localized band of lattice defects, which nucleates in the near surface region due to incomplete dynamic annealing during ion bombardment.

3.3. Impurity lattice site location using β^- emission channeling

Figures 5(a)–(d) show the experimental emission patterns along the [0001], [$\bar{1}$102], [$\bar{1}$101] and [$\bar{2}$113] directions of sample S1 following 300 °C annealing. Figures 5(e)–(h) show the best fits of the corresponding theoretical yields, obtained

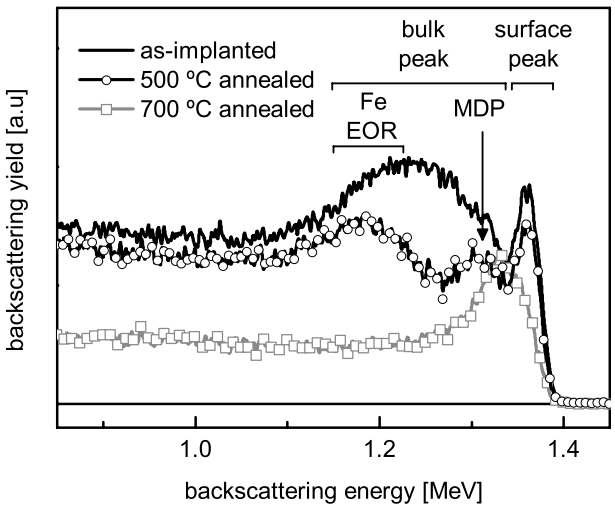

Figure 4. RBS/C spectra measured in glancing geometry (15° exit angle with respect to the sample surface) in the channeling orientation of sample S10 (1×10^{16} cm^{-2}) for the different annealing stages. Four different damage regions are indicated: surface peak, bulk peak and, within the bulk peak, the region corresponding to the Fe end of range (EOR) and the middle defect peak (MDP).

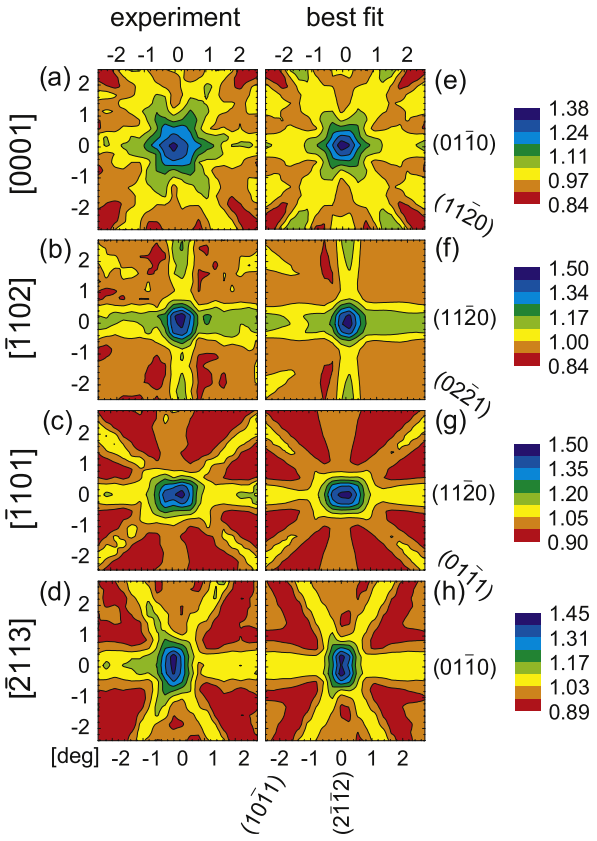

Figure 5. (a)–(d) Normalized experimental emission patterns along the [0001], [$\bar{1}$102], [$\bar{1}$101] and [$\bar{2}$113] directions of sample S1 (1×10^{15} cm^{-2}) following 300 °C annealing. (e)–(h) Corresponding best fits of theoretical yields, obtained by varying the fraction of Fe on substitutional S_{Zn} sites (best fit for a fraction of 77(5)%) and varying its rms displacement u_1 from the ideal S_{Zn} site (best fit for $u_1 = 0.08(1)$ Å).

by varying the fraction of Fe on substitutional S_{Zn} sites (best fit for a fraction of 87(5)%) and varying rms displacement u_1 from the ideal S_{Zn} site (best fit for $u_1 = 0.08(1)$ Å). The remaining Fe fraction contributes with an isotropic emission yield, and is discussed below. Figure 6 compiles the fit results for the different fluences and annealing stages: the fractions of Fe impurities in S_{Zn} are plotted in figure 6(a) and the corresponding rms displacements u_1 in figure 6(b).

3.3.1. Random fraction. The random fractions are virtually independent of annealing temperature and increase with implanted fluence. They correspond to Fe atoms which are located either in (1) crystalline secondary phases which are not coherent with the host structure, or in (2) highly disordered regions. Based on the work of Zhou *et al*, case (1) could correspond to metallic α-Fe nanoclusters. However, these can be excluded based on the SQUID measurements at room temperature, from which we concluded that the maximum Fe fractions in α-Fe nanoclusters was below 1% (see above). We interpret the observed random fraction as case (2), i.e. Fe impurities located in highly disordered (or even amorphous) regions. Because the random Fe fractions are very small and do not induce measurable ferromagnetism, their (potentially) magnetic behavior is assumed in the remainder of this paper to be negligible compared to the net magnetic moment of the substitutional Fe fraction. Note that the random fractions may even be somewhat overestimated, as a result of electron dechanneling due to beam-induced lattice disorder [44–47].

3.3.2. Substitutional Fe. The substitutional fraction consists of Fe atoms occupying sites which are epitaxially aligned with the Zn sublattice along the four measured directions. These sites can either be (1) true Zn sites in the ZnO wurtzite structure or (2) Fe sites in a secondary phase crystallite which are aligned with the Zn sublattice of the host ZnO structure. Even though the crystallites of the spinel ferrite $ZnFe_2O_4$ identified by Zhou *et al* [10, 11] can be crystallographically aligned with the ZnO wurtzite structure, the Fe sublattice in such structures is not coherent with the Zn sublattice of the host ZnO matrix. Hence, we are left with case (1). However, occupying nearly ideal Zn sites in the ZnO wurtzite structure does not necessarily mean that the Fe is uniformly distributed. From the EC results, one can only conclude that the majority of the Fe impurities are located in the cation sites of a wurtzite alloy of formula $Zn_{1-x}Fe_xO$; x may vary locally creating Fe-rich and Fe-poor regions. Such aggregation effects are limited by the mobility of the Fe impurities; although randomly incorporated in the crystal during implantation, they may become mobile and aggregate at sufficiently high annealing temperatures. Because aggregation implies a decrease of the average minimum distance between neighboring Fe impurities, it enhances the magnetic interactions between the Fe localized moments. However, emission channeling is unable to probe the uniformity of the Fe distribution. Aggregation is discussed in detail next, based on the magnetometry measurements.

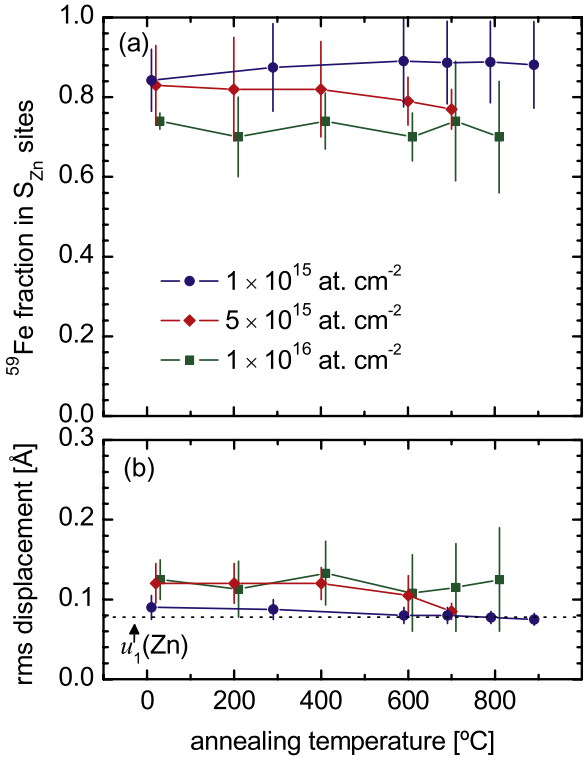

Figure 6. (a) Fractions of ^{59}Fe impurities in Zn-substitutional (S_{Zn}) sites and (b) the corresponding rms displacements u_1 obtained from fitting the experimental patterns with theoretical ones, as described in the text (the dashed line indicates the thermal vibration amplitude of the Zn atoms in the lattice).

However, before analyzing the magnetism in more detail, it is worth discussing the fluence and temperature dependence of u_1. The rms displacement u_1, obtained from fitting the EC patterns, can in principle be divided into two components: the thermal vibration amplitude of Fe impurities in Zn sites, which is expected to be similar to that of the Zn atoms (u_1(Zn) = 0.08 Å) [57], and static displacements from the ideal Zn sites. The fitted u_1 values, plotted in figure 6(b), show that the degree of displacement from ideal Zn sites, and thus the disorder in the vicinity of the Fe impurities, increases with fluence, as expected and observed in the RBS/C data. More importantly, it shows that the disorder in the close vicinity of the Fe impurities anneals only between 600 and 800 °C, as u_1 decreases to the thermal vibration amplitude, which is consistent with our previous emission channeling experiments on very low fluence Fe-implanted ZnO [48]. Combined with the RBS/C results above, this provides a quite detailed insight into the overall damage accumulation and annealing in the EOR region. Thermal annealing up to 600 °C efficiently anneals the damage in the region between the Fe EOR and the surface, as shown by the RBS/C data in figure 4. However, most of the damage in the EOR region persists, most likely because it is stabilized by impurity–defect complexes involving the Fe impurities and native point defects created during implantation, slightly displacing the Fe atoms from the ideal Zn sites and thus explaining the u_1 values lying significantly above the thermal vibration amplitude of Zn in ZnO. According to the extensive work of Weyer *et al* using Mössbauer spectroscopy [58–60], these impurity–defect complexes are most likely Zn-vacancy related, which is supported by EPR measurements [61]. Our data suggest that these impurity–defect complexes dissociate upon annealing between 600 and 800 °C: as the complexes dissociate, the lattice defects (Zn sublattice related) are able to diffuse away from the Fe impurities. This is consistent with the RBS/C data in figure 4, where the Zn-sublattice disorder in the EOR region appears to diffuse towards the surface upon annealing at $T > 500$ °C, as discussed above.

3.4. Low-temperature magnetization and correlation with the structural properties

Let us start by summarizing the main findings so far:

(i) The EC data show that the large *majority* of Fe impurities occupy Zn sites in the ZnO wurtzite structure, i.e. the implanted layer consists of a single-crystalline wurtzite alloy $Zn_{1-x}Fe_xO$, although Fe aggregation into Fe-rich regions cannot be excluded.

(ii) The absence of measurable room-temperature ferromagnetism (or superparamagnetism) shows that the small fraction of non-substitutional Fe, i.e. the random fraction in the EC analysis, cannot be attributed to known secondary phases in Fe-implanted ZnO, i.e. metallic α-Fe or the spinel ferrite $ZnFe_2O_4$.

(iii) The RBS/C data show that thermal annealing decreases the degree of disorder of the $Zn_{1-x}Fe_xO$ layer from a dense damage profile to a nearly fully recovered crystal structure. Combining the RBS/C and the EC results, we conclude that point-like native defects created by implantation form impurity–defect complexes with the Fe impurities. Thermal annealing at 600 °C and above induces the dissociation of these complexes, allowing the native defects to diffuse towards the surface.

(iv) The single-crystalline wurtzite alloy $Zn_{1-x}Fe_xO$ does not display room-temperature ferromagnetism in a wide range of defect density.

Two major questions remain unanswered:

(i) If not high-temperature ferromagnetism, what is the magnetic behavior of wurtzite $Zn_{1-x}Fe_xO$ and how does it depend on the density of lattice defects?

(ii) How does thermal annealing affect the uniformity of x across the $Zn_{1-x}Fe_xO$ layer and, in turn, how does that affect the magnetic interaction between substitutional Fe impurities?

Experimentally addressing question (2) is extremely challenging. We show below that addressing question (1) allows us to infer an answer to question (2). In order to answer (1), we will focus on sample S5 (5×10^{15} cm^{-2}) for the following reasons. As we show next, the large number of paramagnetic impurities in the ZnO substrates (relative to the number of implanted Fe ions) dominates the magnetic signal of sample S1 (1×10^{15} cm^{-2}), thus precluding a detailed analysis. On the other hand, due to the lower quality of

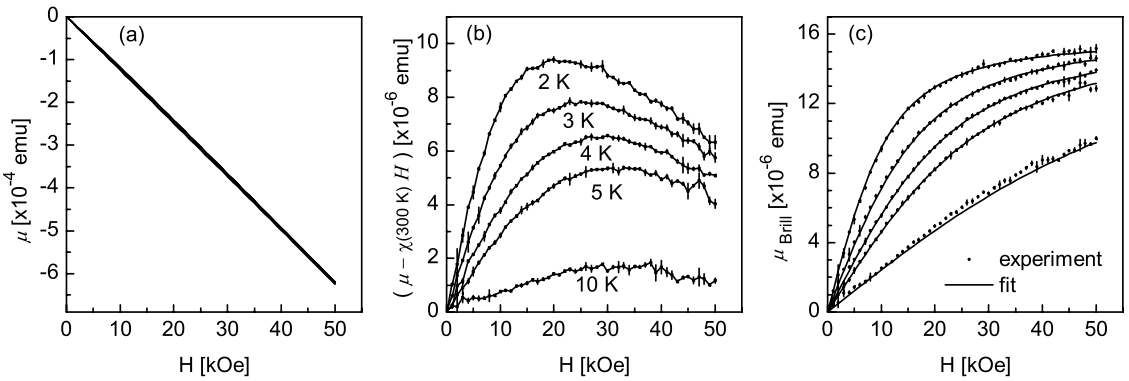

Figure 7. (a) Isothermal *M–H* data of sample S5 prior to implantation at 2, 3, 4, 5, 10 and 300 K (data appear to overlap), measured with decreasing field (from 50 to 0 kOe) parallel to the sample plane. (b) Data after subtraction of the linear component (estimated from the linear fit of the 300 K data in the 20–50 kOe range). (c) Brillouin-like component and corresponding fit, according to the model described in the text.

the EC data of sample S10 (1×10^{16} cm^{-2}), it cannot be determined beyond doubt if the damage in the vicinity of the Fe impurities is completely annealed, making sample S10 less suitable for investigating possible changes in magnetic behavior upon dissociation of the impurity–defect complexes. In addition, if the Fe impurities do aggregate, this should occur at lower annealing temperatures in S10 due to the higher Fe concentration, which makes it more difficult to separate the effects of defect annealing and Fe aggregation on the magnetometry data.

In the following, we analyze the magnetometry data of sample S5 at low temperatures, focusing on the relevant processing stages: prior to implantation, in order to characterize the magnetic background of the ZnO substrate; as-implanted, when the uniformity of the Fe distribution should be maximum; after 500 °C annealing, when most of the damage which does not overlap with the Fe profile has been removed; and after 700 °C annealing, when most of the defects which more directly interact with the Fe impurities have been removed.

3.4.1. As-grown ZnO substrate. Before analyzing the data for the implanted sample, it is necessary to carefully characterize the substrate background. Figure 7(a) shows the isothermal *M–H* data of sample S5 prior to implantation at several temperatures from 2 to 300 K (all data appear to overlap). The nonlinear component of the *M–H* curves at low temperatures is revealed (figure 7(b)) after subtracting the (diamagnetic) linear component at 300 K estimated from the linear fit of the high-field range (20–50 kOe). The shape of these curves resembles a paramagnetic component (following the Brillouin function) superimposed on a small negative slope. The Brillouin-like component can be attributed to paramagnetic impurities, most likely transition metal impurities in the ppm range incorporated during hydrothermal growth [62]. The negative slope at low temperature can be explained by a decreasing van Vleck paramagnetic susceptibility of the ZnO substrate with decreasing temperature (from 300 to $\leq$10 K), due to the temperature dependence of the ZnO bandgap E_g. This has been observed in a number of semiconductor materials and is discussed in some detail in [63] for GaAs substrates. The low-temperature data can therefore be fitted using the *ansatz*

$$\mu(H,T) = \mu_{\mathrm{Brill}}(H,T) + \Delta\mu_{\mathrm{vV}}^{\mathrm{ZnO}}(H,T), \qquad (1)$$

where μ_{Brill} is the Brillouin-like magnetic moment of the paramagnetic impurities and $\Delta\mu_{\mathrm{vV}}^{\mathrm{ZnO}}$ accounts for the variation of the van Vleck paramagnetic susceptibility of the ZnO substrate. The Brillouin-like component can be expressed as

$$\mu_{\mathrm{Brill}}(H,T) = NgJ\mu_{\mathrm{B}}B_J(x), \qquad \left(x \equiv \frac{gJ\mu_{\mathrm{B}}H}{k_{\mathrm{B}}T}\right), \quad (2)$$

where N is the number of paramagnetic impurities, g is the Landé factor, J is the total angular momentum quantum number and $B_J(x)$ is the Brillouin function:

$$B_J(x) = \frac{2J+1}{2J}\coth\left(\frac{2J+1}{2J}x\right) - \frac{1}{2J}\coth\left(\frac{1}{2J}x\right). \quad (3)$$

Assuming that the orbital momentum L is fully quenched ($L = 0$), which we show below to be a good approximation in this case, J is given by the spin quantum number S ($J = S$) and $g = 2.00$. To a first approximation, we can assume that the van Vleck paramagnetic susceptibility varies very little from 10 to 2 K, so that $\Delta\mu_{\mathrm{vV}}$ can be taken as

$$\Delta\mu_{\mathrm{vV}}^{\mathrm{ZnO}}(H,T) = \Delta\chi_{\mathrm{vV}}^{\mathrm{ZnO}}H, \qquad (4)$$

where $\Delta\chi_{\mathrm{vV}}^{\mathrm{ZnO}}$ is independent of temperature and field. Figure 7(c) shows the data in (b) and the fit using the described *ansatz*, with S, N and $\Delta\chi_{\mathrm{vV}}^{\mathrm{ZnO}}$ as free parameters. The fit reproduces the data quite well, with $S = 2.6(2)$, $N = 3.11(3)$ (i.e. a concentration of 4×10^{16} cm^{-3}) and $\Delta\chi_{\mathrm{vV}}^{\mathrm{ZnO}}$ corresponding to about 1% of the diamagnetic susceptibility at 300 K. The Brillouin component is consistent with Fe^{3+} (d^5 $S = 5/2$), a common impurity in hydrothermally grown ZnO [64], particularly in the substrates used here (grown by CrysTec GmbH) [62]. The small $\Delta\chi_{\mathrm{vV}}^{\mathrm{ZnO}}$ is consistent with the expected small temperature dependence of the van Vleck paramagnetic susceptibility. Note that all the data are fitted simultaneously, i.e. the same N, S and $\Delta\chi_{\mathrm{vV}}^{\mathrm{ZnO}}$ values are optimized simultaneously for the different temperatures.

The derivation of the Brillouin function does not take into account anisotropic crystal fields. In wurtzite materials

such as ZnO, substitutional impurities are subject to a trigonal crystal field. Via the spin–orbit interaction, this anisotropic crystal field induces a strong magnetic anisotropy, which can be described by a zero-field splitting of the fundamental state and by an anisotropic effective g-factor in an effective spin Hamiltonian H_s of the form

$$H_s = \mu_B g_{\parallel} H_z S_z + \mu_B g_{\perp}(H_x S_x + H_y S_y) + D S_z^2, \qquad (5)$$

where S is the spin quantum number, D describes the zero-field splitting, and $g_{\parallel}$ and $g_{\perp}$ are the effective g-factors for directions of magnetic field parallel and perpendicular to the wurtzite c-axis, respectively. Therefore, in general, the $\mu(H, T)$ behavior of paramagnetic impurities in the crystal field of the ZnO wurtzite lattice cannot be correctly reproduced by the Brillouin function. The fact that it does in our case shows that the zero-field splitting constant for this particular impurity in ZnO is very small. This is typically the case for $S = 5/2$ moments (e.g. $D = -0.0074$ meV for Fe^{3+} d^5 in ZnO [65], $D = -0.0027$ meV for Mn^{2+} d^5 in ZnO [66] and $D = -0.0093$ meV for Mn^{2+} d^5 in GaN [67]). In fact, even for Co^{2+} (d^7, $S = 3/2$), where D is significantly larger (0.342 meV), the in-plane magnetization can be reasonably well described by the Brillouin function [25].

Because the implantation affects only a very thin layer of less than 1/1000 of the whole substrate thickness, this substrate background can be taken as unchanged after implantation, allowing us to isolate the magnetization associated with the implanted Fe impurities and beam-induced defects.

3.4.2. After implantation at room temperature. Figure 8(a) shows the low-temperature M–H curves of sample S5 in the as-implanted state, after subtraction of the diamagnetic component estimated from the linear fit of the high-field (10–20 kOe) magnetization at 300 K. Fitting the data with the same *ansatz* (1) gives a reasonable agreement (figure 8(b)). To be more precise, the data are fitted to a sum of two terms of the form of (1): for one of them, the parameters N, S and $\Delta\chi_{vV}^{ZnO}$ are set (i.e. fixed) to those obtained prior to implantation (i.e. due to the contaminant paramagnetic background), so that the free N, S and $\Delta\chi_{vV}^{ZnFeO}$ parameters of the second term describe the implanted layer. The agreement can be further improved by allowing $\Delta\chi_{vV}^{ZnFeO}$ to be temperature dependent, which is implemented in the fitting as follows. First, the 2 K M–H curve, which carries more 'information' as it provides a wider range of H/T (and thus of x in equation (2)), is fitted with N, S and $\Delta\chi_{vV}^{ZnFeO}$ as free parameters. The M–H curves for 5 and 10 K are then fitted separately, fixing the N and S values determined from the 2 K M–H, and varying only $\Delta\chi_{vV}^{ZnFeO}$. Figure 8(b) compares the experimental data to the best fit, after subtraction of $\Delta\chi_{vV}^{ZnFeO}H$ in order to more clearly show the Brillouin component. The agreement is again very good, supporting the existence of two types of paramagnetism: Brillouin-like and van Vleck-like.

- Brillouin-like component. The best fit is obtained for $S = 2.5(1)$, i.e. $S = 5/2$ within the error, which is the expected behavior for the implanted Fe if it is incorporated as Fe^{3+} d^5. The zero-field splitting D for Fe^{3+} d^5 is sufficiently small (-0.0074 meV) [65] for the Brillouin function to be a good approximation. Although 2+ is the 'neutral' charge state of Fe impurities substituting group-II Zn in ZnO, a 3+ charge state may result from charge transfer from neighboring acceptor defects. It has been suggested, based on Mössbauer experiments, that Fe impurities in impurity–defect complexes with Zn vacancies (acceptors) created during Fe implantation are indeed in the 3+ charge state [58–60]. This is also supported by EPR measurements [61], and is consistent with our RBS/C and EC results discussed above, which also indicate the

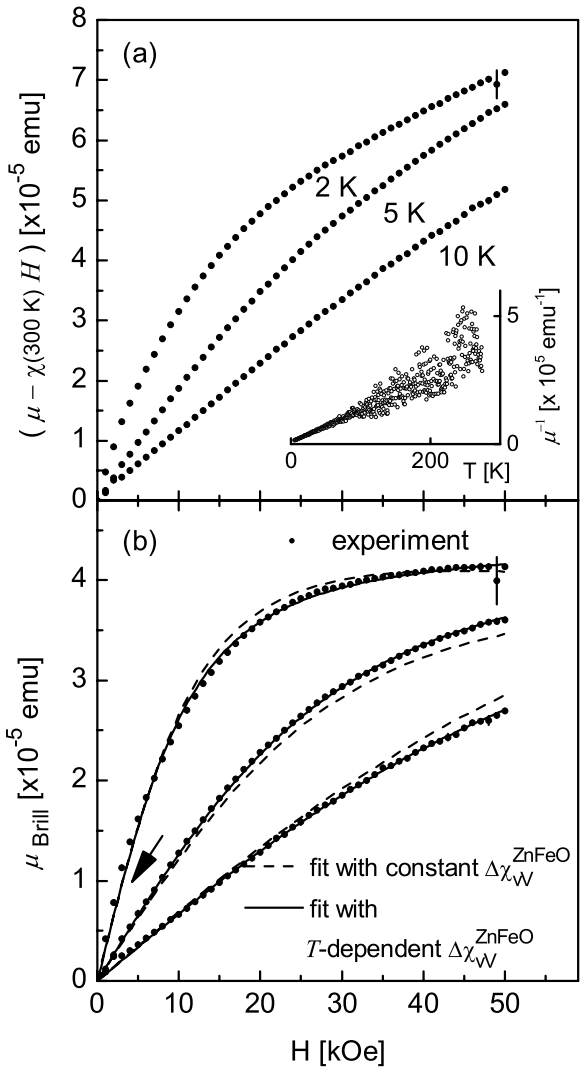

Figure 8. (a) Isothermal M–H data of sample S5 in the as-implanted state, at 2, 5 and 10 K, corrected for the diamagnetic susceptibility at 300 K (*inset*: M–T data of the same sample, with an applied field of 50 kOe, corrected of the diamagnetic component following the procedure described in [34], and plotted as $\mu^{-1}(T)$ in order to show the paramagnetic Curie behavior). (b) Brillouin-like component of the experimental data and corresponding theoretical fits according to the model described in the text. The best fit is obtained for $S = 5/2$, with $\Delta\chi_{vV}^{ZnFeO}$ taken as temperature independent (dashed line) or temperature dependent (solid line). The arrow indicates the region of poor fit *even* when $\Delta\chi_{vV}^{ZnFeO}$ is allowed to vary.

formation of such complexes. The perturbation induced by the neighboring native defects on the crystal field is extremely small (of the order of 10^{-6} meV [61]) and, therefore, the Brillouin function remains a good approximation.

The small deviations from the Brillouin fit (arrow in figure 8(b)) can be attributed to a small fraction of the implanted Fe impurities in the 2+ charge state. In principle one could attempt to incorporate such a fraction in the fit. However, D, $g_{\parallel}$ and $g_{\perp}$ (equation (5)) are unknown for Fe^{2+} in ZnO, which would require too many free parameters in the fit. For Mn^{3+} in GaN, in principle a very similar case ($S = 2$), $D = 0.27$ meV [68], i.e. sufficiently high to induce the observed deviations from Brillouin behavior in figure 8(b).

Another important observation concerns the fitted number of paramagnetic centers $N = 5.6(4) \times 10^{14}$, i.e. only about 45% of the number of implanted Fe impurities. The decreased N can in part be attributed to fitting the data with a high spin Fe^{3+} d^5 ($S = 5/2$), when a fraction may in fact be Fe^{2+} d^6 ($S = 2$). In addition, it is possible that the magnetic moment of Fe impurities in highly damaged regions (the random fraction in EC, i.e. 16% of the implanted Fe) may be quenched. However, even these two effects combined are insufficient to explain the 'missing' 55% of the Fe impurities. This suggests an additional source of Fe moment quenching: the mutual compensation of the magnetic moment of neighboring Fe impurities due to the antiparallel alignment of their spins, imposed by strong nearest-cation-neighbor antiferromagnetic interactions. Even if the Fe impurities are randomly incorporated in Zn sites in ZnO upon implantation, there is a finite fraction that occupies nearest-cation-neighbor sites: 34% according to the Behringer equation [69] taking with $x = x_p$. If the magnetic interaction between neighboring Fe moments is antiferromagnetic, the resulting antiparallel alignment of their spins renders this fraction 'invisible' in the magnetization data. A similar moment-compensation effect has been observed in other DMS systems, e.g. Co-doped ZnO [27, 28] and Cr-doped GaN [34].

- van Vleck-like component. There is an important observation, independent of any fitting, which we have not mentioned so far: the total magnetic moment at 2 K and 50 kOe (figure 8(a)) of 7.1×10^{-5} emu, is larger than that expected from the Fe impurities even if all were to contribute with the maximum spin-only value of 5 μ_B (5.8×10^{-5} emu in total), even more so, as the curve seems to be far from saturation. There is then an additional contribution from paramagnetic defects in the implanted layer other than the Fe impurities. The fitting presented above indicates that this additional contribution can be described by a van Vleck-like paramagnetic susceptibility of the form

$$\chi_{vV}^{ZnFeO}(T) = \frac{\mu_{vV}^{ZnFeO}(H,T)}{H} = \chi_{vV}^{ZnFeO}(300\ \mathrm{K}) + \Delta\chi_{vV}^{ZnFeO}(T). \quad (6)$$

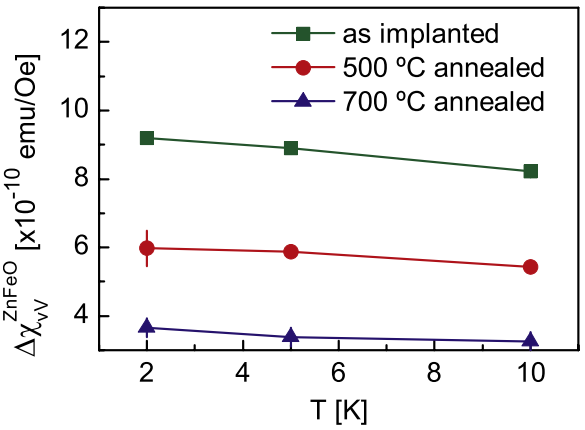

Figure 9. Measurement temperature and annealing temperature dependence of $\Delta\chi_{vV}$ (equation (4)), obtained from fitting the low-temperature M–H data of sample S5.

We attribute this van Vleck-like paramagnetic component to native defects created during implantation, which is further supported as we analyze the changes induced by annealing, below. The temperature dependence of $\Delta\chi_{vV}^{ZnFeO}$ is shown in figure 9. This van Vleck-like susceptibility component decreases with increasing temperature, which is the opposite to what was observed above for the van Vleck susceptibility of the substrate $\Delta\chi_{vV}^{ZnO}$ (due to the temperature dependence of the bandgap), and therefore supports their distinct origins ($\Delta\chi_{vV}^{ZnO}$ from the perfect crystal, and $\Delta\chi_{vV}^{ZnFeO}$ from the beam-induced damage). It is, however, very difficult to estimate the absolute magnitude of either van Vleck-like susceptibilities, since it is virtually impossible to separate it from the purely (Langevin-like) diamagnetic susceptibility solely based on our data. Moreover, it is possible that part of the fitted $\Delta\chi_{vV}^{ZnFeO}$ component originates, in fact, from the antiferromagnetically coupled Fe impurities, contributing with a non-vanishing (antiferro)magnetic susceptibility. In any case, as discussed above, a source of van Vleck-like magnetization must exist, since the Fe impurities alone cannot account for the magnitude of the observed magnetization. However, the detailed description of such defect-related van Vleck paramagnetism and its temperature dependence is beyond the scope of this work.

3.4.3. Following 500 °C annealing. Following 500 °C annealing, the M–H data are still relatively well reproduced by the model above (figure 10(a)), though clearly not as well as for the as-implanted state. Compared to the as-implanted state, although the fitted $S = 2.4(6)$ remains unchanged within the error, the error itself increases significantly (from 0.1 to 0.6). In addition, N decreases to $3.6(6) \times 10^{14}$. This indicates that one or both of the following modifications occurred upon annealing: (1) part of the Fe^{3+} fraction was converted to Fe^{2+} due to partial annealing of defects; (2) part of the isolated (magnetically active) Fe impurities suffered short-range diffusion and formed pairs or larger complexes with other Fe impurities (thus contributing with a vanishingly

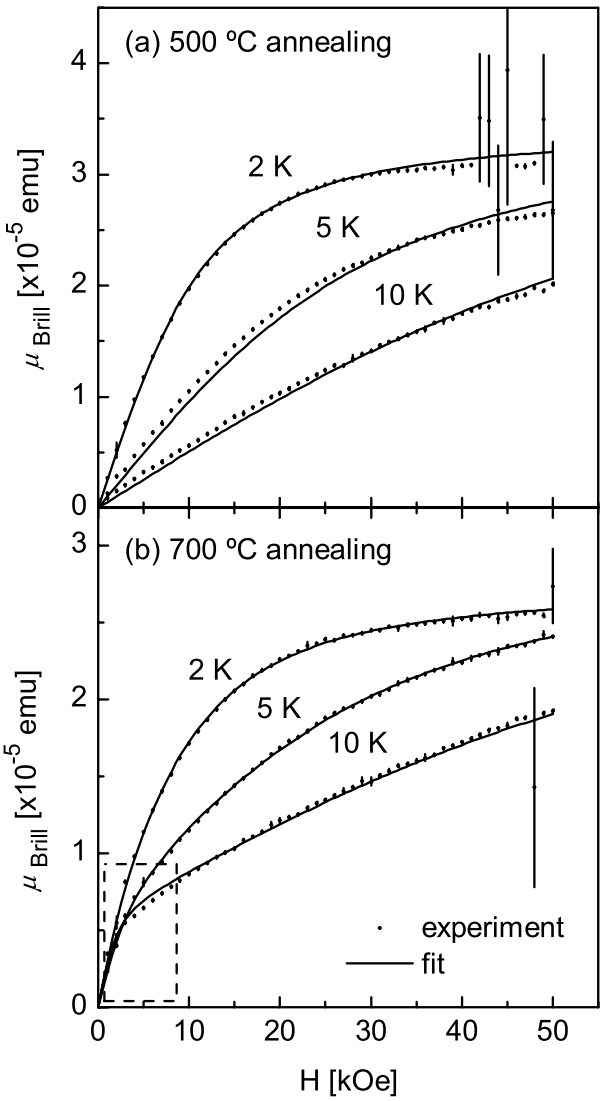

Figure 10. Brillouin-like component of the isothermal *M–H* data at 2, 5 and 10 K of sample S5 and corresponding theoretical fits (models described in the text): (a) following 500 °C annealing; (b) following 700 °C annealing.

small moment). As we show below, the analysis of the data corresponding to the next annealing step indicates that, in fact, both (1) and (2) occurred. Note that also the van Vleck-like component $\Delta\chi_{vV}^{ZnFeO}$ decreased with annealing (figure 9), which is consistent with the decrease in defect density as probed by RBS/C.

3.4.4. Following 700 °C annealing. Fitting the 700 °C data with the same model, i.e. with only one S value for the implanted Fe component, gives $S = 5.8(4)$, i.e. more than twice the maximum spin-only value of 5/2 for a 3*d* moment. This indicates the formation of sufficiently large complexes where, although antiferromagnetic interactions may dominate, frustration effects or uncompensated spins result in a non-vanishing net moment. Lacking a better (and still simple) description of such a system, it is worthwhile attempting to fit the data with a model simply based on Brillouin-like paramagnetism. This can be done by allowing

Table 2. Best fit parameters of the Brillouin component of the low-temperature *M–H* data of sample S5, obtained using the models described in the text.

	S	N ($\times 10^{14}$)	S_2	N_2 ($\times 10^{14}$)
As-implanted	2.5(1)	5.6(4)	—	—
500 °C annealed	2.4(6)	3.6(6)	—	—
700 °C annealed	1.8(7)	1.8(7)	9(3)	0.2(1)

two Brillouin-like fractions with the corresponding N, N_2, S and S_2 free parameters, in addition to $\Delta\chi_{vV}^{ZnFeO}$. Figure 10(b) compares the experimental data to the best fit obtained using such a model, i.e. introducing a second Brillouin component with the corresponding N_2 and S_2 parameters free at all temperatures. The best fit of the 2 K data is obtained for $S = 1.8(7)$ and 9(3). For the 5 and 10 K data, the best fit S_2 values vary considerably, up to $S = 70(15)$, showing that the large-S fraction is in fact very poorly described by the Brillouin function. Nevertheless, this analysis indeed suggests that part of the Fe impurities aggregate in larger complexes. In fact, this can be inferred independently of any fit, from the increase in low-field susceptibility (dashed rectangle in figure 10) without an increase in saturation moment. In addition, the decrease of the small-S component from $S = 2.4(6)$ to $S = 1.8(7)$ (although with a large error), suggests that part of the isolated Fe^{3+} d^5 ($S = 5/2$) fraction may have been converted to Fe^{2+} d^6 ($S = 2$).

Regarding the van Vleck-like component $\Delta\chi_{vV}^{ZnFeO}$, it is greatly decreased after 700 °C annealing (figure 9), consistent with further damage recovery. This is discussed in more detail below.

4. Discussion

We will now summarize and discuss the magneto-structural analysis presented above, dividing it into four main effects. First and most important, Zn-substitutional Fe impurities in ZnO are paramagnetic when isolated and interact antiferromagnetically when in nearest-cation-neighbor complexes. Second, under the implantation and annealing conditions that we used, the aggregation of Zn-substitutional Fe impurities in ZnO occurs without the segregation of a secondary phase. Third, Fe implantation creates a van Vleck-like paramagnetic component which we suggest to originate from the defects created upon irradiation. In a fourth and last point of discussion, we will comment on the absence of ferromagnetism in Fe-implanted ZnO, from the perspective of the various mechanisms of ferromagnetic order in wide-gap DMS proposed so far.

4.1. Paramagnetism and antiferromagnetic interactions

Table 2 compiles the parameters obtained from fitting the low temperature *M–H* data using the model described above. Combined with the RBS/C and EC results, the magneto-structural behavior of Fe impurities in ZnO can be summarized as follows.

Upon implantation, the vast majority of the Fe impurities are more or less randomly incorporated in Zn-substitutional sites (i.e. region (1) of the single-phase region of the phase diagram, figure 1). A significant fraction of these Fe impurities form impurity–defect complexes with neighboring native point defects, most likely Zn vacancies (acceptors), assuming a 3+ charge state and a d^5 ($S = 5/2$) paramagnetic moment. The formation of such impurity–defect complexes in Fe-implanted ZnO, and the resulting 3+ charge state of the Fe impurities has been established by the extensive Mössbauer spectroscopy work of Weyer *et al* [58–60].

Thermal annealing at moderate temperatures (∼500 °C) has two parallel effects on the paramagnetic Fe impurities: (i) thermally activated dissociation of part of the impurity–defect complexes; (ii) the increased mobility of the Fe impurities at moderated temperatures allows part of the Fe impurities to diffuse across short distances and form substitutional Fe–Fe dimers. This state can be regarded as an intermediate region between regions (1) and (2) of the single-phase region of the phase diagram, figure 1. Based on the decrease in N from $5.6(4) \times 10^{14}$ to $3.6(6) \times 10^{14}$, we estimate that about one third of the isolated Fe impurities form dimers, where strong nearest-cation-neighbor antiferromagnetic interactions impose the antiparallel alignment of the Fe spins, resulting in a vanishingly small net magnetic moment per complex. As mentioned above, a similar moment-compensation effect has been observed in other DMS systems, e.g. Co-doped ZnO [27, 28] and Cr-doped GaN [34].

Thermal annealing at higher temperatures (∼700 °C) accelerates both (thermally activated) processes (i) and (ii) mentioned in the previous paragraph. The Zn-sublattice defects in the vicinity of the Fe impurities are annealed (i), and the fraction of paramagnetic Fe decreases to a third of that in the as-implanted state (ii), due to Fe aggregation and resulting magnetic compensation. However, unlike after the 500 °C annealing, the decrease in the isolated Fe fraction cannot be attributed to dimer formation alone. A high-spin fraction also appears (with S_2 and N_2), corresponding to about 40% of the Fe-related magnetization, which we attribute to Fe aggregates larger than dimers (i.e. with more than two Fe atoms per complex). These aggregates can be regarded as regions of the $Zn_{1-x}Fe_xO$ layer where x is significantly larger than x_p and approaches 1. This aggregation state corresponds to region (2) of the single-phase region of the phase diagram, figure 1. In such substitutional Fe aggregates, strong nearest-cation-neighbor antiferromagnetic interactions favor the antiparallel alignment of the Fe spins. However, due the lack of translation symmetry (random Zn/Fe cation-site occupation) of such structures as well as their finite size, frustration effects and uncompensated spins result in a non-vanishing net moment per complex.

4.2. Fe aggregation and segregation mechanisms

Based on the EC and magnetization data, we have excluded the formation of significant fractions of any magnetic secondary phase from the as-implanted state up to 900 °C annealing (i.e. we remained in regions (1) and (2) of the single-phase region of the phase diagram, figure 1). This appears to be inconsistent with the findings of Zhou *et al* [11], who, for similar Fe concentrations reported that significant fractions of the implanted Fe impurities segregate in superparamagnetic secondary phases: metallic α-Fe nanoprecipitates at processing temperatures of about 500–800 °C (region (3) in figure 1), and in spinel ferrite $ZnFe_2O_4$ nanoprecipitates at processing temperatures above ∼800 °C (region (4) in figure 1). Instead, in our samples, nearly all Fe impurities (>70%) substitute for Zn in the ZnO wurtzite structure and, in addition, no superparamagnetic fraction is observed within the sensitivity of our SQUID measurements (<1%). In other words, in our samples, thermal annealing simply promoted the aggregation of Zn-substitutional Fe impurities into Fe-rich regions of the wurtzite $Zn_{1-x}Fe_xO$ -implanted layer. We suggest that this apparent discrepancy results from different defect accumulation mechanisms. Lattice defects, either point-like or extended, affect the diffusivity of the Fe impurities and, therefore, may lead to different Fe segregation mechanisms. The differences in defect accumulation, on the other hand, may originate from a combination of (i) different implantation parameters (ion energy, current density, implantation temperature) and (ii) different initial conditions of the implanted ZnO materials in terms of crystalline quality. Indeed, Zhou *et al* have shown that the segregation of the implanted Fe impurities is very sensitive to the ZnO crystallinity prior to implantation: the formation of α-Fe clusters [11, 10] was suppressed by annealing the ZnO substrates prior to implantation [9, 12]; bulk ZnO substrates and epitaxial ZnO thin films showed very distinct segregation behaviors [11].

4.3. van Vleck-like paramagnetism associated with beam-induced damage

The fit parameter $\Delta\chi_{vV}^{ZnFeO}$, at 2 K, is plotted in figure 11 as a function of annealing temperature, normalized to its maximum value in the as-implanted state. In an attempt to identify from which type (or region) of defects the van Vleck-like paramagnetic component originates, figure 11 compares $\Delta\chi_{vV}^{ZnFeO}$ to the bulk and surface minimum yield χ_{min} as well as the number of Fe^{3+} (N in the Brillouin-like fits above), which is in principle a measure of the number of lattice defects involved in the Fe^{3+}–defect complexes. All data sets overlap within the experimental error, which is quite remarkable considering that very different quantities are compared. However, though strongly supporting the defect-related origin of the van Vleck-like susceptibility, this comparison is unable to discern which of the defect components is involved. Further experimental and theoretical work will be necessary in order to elucidate the exact origin of this van Vleck-like paramagnetism.

4.4. Lack of ferromagnetic order in single-phase $Zn_{1-x}Fe_xO$

Our main finding is essentially the absence of ferromagnetic order in single-phase $Zn_{1-x}Fe_xO$, for a wide range of

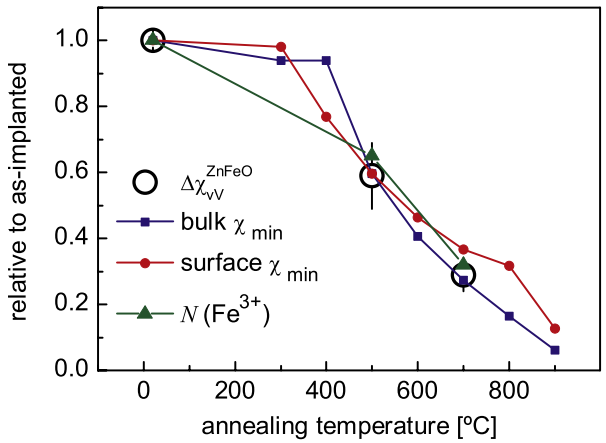

Figure 11. Dependence on annealing temperature of $\Delta\chi_{vV}^{ZnFeO}$ at 2 K, compared to the quantities associated with its potential sources, i.e. the quantities associated with the various types (or regions) of defects which may originate the van Vleck-like paramagnetism. Bulk and surface χ_{min} are a measure of the defects in the bulk and surface regions, respectively. The number N of Fe^{3+} impurities (N in the Brillouin-like fits) is a measure of the amount of defects involved in the Fe^{3+}–defect complexes. All values are normalized to the respective maximum value, i.e. in the as-implanted state.

Fe concentration x and density of lattice defects. The effects of magnetic interactions can be inferred from the magnetization data, but that interaction is antiferromagnetic and short-ranged. Similar behavior has been observed for Co impurities in ZnO [27, 28, 31, 32], which is consistent with the antiferromagnetic nature of the corresponding oxides FeO and CoO, with Néel temperatures of 198 and 291 K [70], respectively. This suggests that the localized 3d moments of Fe impurities in ZnO can only interact through indirect superexchange via the O 2p band, thus excluding any of the mechanisms of long-range ferromagnetic order so far proposed for wide-gap DMS. $Zn_{1-x}Fe_xO$ being a fairly representative example of wide-gap DMS systems, it is worthwhile discussing why such mechanisms fail to produce ferromagnetic order.

Carrier-mediated ferromagnetism, e.g. via p–d Zener exchange [19], is easily excluded since, unlike Mn in GaAs and InAs, Fe impurities do not introduce the required free carriers in ZnO (p-holes in the Zener case).

As an alternative to carrier-mediated mechanisms, high-temperature ferromagnetism in wide-gap DMS materials has also been proposed on the basis of bound magnetic polarons (BMP) [36]. Here, the magnetic moments interact via electrons of an impurity band associated with lattice defects, such as those created during implantation. However, the exchange energy density necessary to produce high-temperature ferromagnetism with a few % of transition metal doping corresponds to a magnetic exchange much stronger than that observed in the strongest known ferromagnetic materials [37]. The lack of such strong magnetic exchange is most likely the reason why we did not observe BMP ferromagnetism down to 2 K, even though we considerably varied the density of *beam-induced* defects in the $Zn_{1-x}Fe_xO$ layers.

A different type of model has been proposed that does not rely on ordered 3d local moments and Heisenberg-type exchange as in p–d Zener exchange and BMP mechanisms: charge transfer ferromagnetism (CTF) [37], which can be considered a Stoner-type mechanism. CTF requires two distinct types of defects, one that creates a narrow impurity band and another to play the role of a charge reservoir. If both types of defects are present, electrons can be transferred to or from the reservoir until the filling level of the impurity band satisfies the spontaneous spin-split criterion. In dilute magnetic semiconductors, the impurity band can originate, for example, from grain boundaries or beam-induced defects, while mixed-valency impurities may behave as charge reservoirs. However, although Fe and other 3d transition metals have indeed more than one charge state within the ZnO bandgap, our results suggest that the types of defects produced during implantation do not to satisfy the stringent requirements for the role of the impurity band.

All the mechanisms discussed above (p–d Zener exchange, BMP, CFT and related ones) belong to a general class of *collective* ferromagnetism and, as such, face a general obstacle in the context of wide-gap DMS: the lack of an efficient mediator of long-range order. An alternative scheme has been proposed in which magnetoelastic effects lead to anisotropy-driven magnetic order in the absence of exchange, i.e. single-ion anisotropy and single-ion magnetism [71, 72]. Indeed, magnetoelastic spin ordering has been proposed to be the origin of the high-temperature ferromagnetic-like behavior in transition metal doped $SrTiO_3$ [73–76]. In Fe-doped ZnO, on the other hand, such magnetoelastic spin order has not been observed, most likely because the required Jahn–Teller effect is absent or too weak [71]. In ZnO, Fe impurities (in Zn sites, with tetrahedral coordination) are Jahn–Teller ions only if in the 2+ charge state [71], and, even then, Fe^{2+} ions typically have very low Jahn–Teller energies [77].

5. Conclusions

The comprehensive description of wide-gap DMS materials requires a detailed assessment of how dilute magnetic moments behave in a non-magnetic host, from the point of view of structure and magnetism, as well as the correlation between the two. When doing so, one of the main challenges is to identify the growth or doping conditions which lead to single-phase materials, in which the true DMS behavior can be investigated.

We have shown that, in single-phase $Zn_{1-x}Fe_xO$ prepared by ion implantation, isolated Fe impurities occupy Zn-substitutional sites and behave as localized paramagnetic moments down to 2 K, irrespective of Fe concentration and the density of beam-induced defects. With increasing local Fe concentration, short-range antiferromagnetic interactions favor the antiparallel alignment of the localized Fe moments, resulting in an efficient moment compensation.

Together with recent comprehensive studies on single-phase transition metal doped ZnO and other wide-gap semiconductors, our findings support the view that the absence of *collective* ferromagnetism is a general feature of wide-gap DMS, resulting from the lack of an efficient

mediation mechanism for long-range interaction. This notion suggests that the search for high-temperature ferromagnetism in wide-gap DMS may be more successful if exploring single-ion magnetism, such as anisotropy-driven magnetic order induced by magnetoelastic effects.

Acknowledgments

This work was supported by the Portuguese Foundation for Science and Technology (CERN/FP/123585/2011, SFRH/BD/35761/2007), the European Union Seventh Framework through ENSAR (European Nuclear Science and Applications Research, Contract No. 262010) and SPIRIT (Support of Public and Industrial Research Using Ion Beam Technology, Contract No. 227012), the Fund for Scientific Research—Flanders, and KU Leuven Projects No. GOA/2009/006 and GOA/2014/007.

References

[1] Dietl T 2010 *Nature Mater.* **9** 965
[2] Pereira L M C, Araujo J P, Van Bael M J, Temst K and Vantomme A 2011 *J. Phys. D: Appl. Phys.* **44** 215001
[3] Abraham D W, Frank M M and Guha S 2005 *Appl. Phys. Lett.* **87** 252502
[4] Ney A, Kammermeier T, Ney V, Ollefs K and Ye S 2008 *J. Magn. Magn. Mater.* **320** 3341
[5] Garcia M A, Fernandez Pinel E, de la Venta J, Quesada A, Bouzas V, Fernandez J F, Romero J J, Martin Gonzalez M S and Costa-Kramer J L 2009 *J. Appl. Phys.* **105** 013925
[6] Sawicki M, Stefanowicz W and Ney A 2011 *Semicond. Sci. Technol.* **26** 064006
[7] Sun Z *et al* 2008 *Phys. Rev.* B **77** 245208
[8] Martinez-Criado G, Somogyi A, Ramos S, Campo J, Tucoulou R, Salome M, Susini J, Hermann M, Eickhoff M and Stutzmann M 2005 *Appl. Phys. Lett.* **86** 131927
[9] Potzger K, Zhou S, Reuther H, Kuepper K, Talut G, Helm M, Fassbender J and Denlinger J D 2007 *Appl. Phys. Lett.* **91** 062107
[10] Zhou S, Potzger K, Reuther H, Talut G, Eichhorn F, von Borany J, Skorupa W, Helm M and Fassbender J 2007 *J. Phys. D: Appl. Phys.* **40** 964
[11] Zhou S *et al* 2008 *J. Appl. Phys.* **103** 023902
[12] Zhou S *et al* 2008 *J. Phys. D: Appl. Phys.* **41** 105011
[13] Zhou S, Potzger K, von Borany J, Grotzschel R, Skorupa W, Helm M and Fassbender J 2008 *Phys. Rev.* B **77** 035209
[14] Zhou S, Potzger K, Kuepper K, Grenzer J, Helm M, Fassbender J, Arenholz E and Denlinger J D 2008 *J. Appl. Phys.* **103** 043901
[15] Borges R P, Ribeiro B, Costa A R G, Silva C, da Silva R C, Evans G, Goncalves A P, Cruz M M and Godinho M 2011 *Eur. Phys. J.* B **79** 185
[16] Ney A, Kovacs A, Ney V, Ye S, Ollefs K, Kammermeier T, Wilhelm F, Rogalev A and Dunin-Borkowski R E 2011 *New J. Phys.* **13** 103001
[17] Ney A *et al* 2010 *New J. Phys.* **12** 013020
[18] Matsumoto Y, Murakami M, Shono T, Hasegawa T, Fukumura T, Kawasaki M, Ahmet P, Chikyow T, Koshihara S and Koinuma H 2001 *Science* **291** 854
[19] Dietl T, Ohno H, Matsukura F, Cibert J and Ferrand D 2000 *Science* **287** 1019
[20] Pearton S J, Abernathy C R, Norton D P, Hebard A F, Park Y D, Boatner L A and Budai J D 2003 *Mater. Sci. Eng.* R **40** 137
[21] Prellier W, Fouchet A and Mercey B 2003 *J. Phys.: Condens. Matter* **15** R1583
[22] Pearton S J, Heo W H, Ivill M, Norton D P and Steiner T 2004 *Semicond. Sci. Technol.* **19** R59
[23] Liu C, Yun F and Morkoc H 2005 *J. Mater. Sci., Mater. Electron.* **16** 555
[24] Stefanowicz W *et al* 2010 *Phys. Rev.* B **81** 235210
[25] Ney A, Kammermeier T, Ollefs K, Ye S, Ney V, Kaspar T C, Chambers S A, Wilhelm F and Rogalev A 2010 *Phys. Rev.* B **81** 054420
[26] Granville S, Ruck B J, Budde F, Trodahl H J and Williams G V M 2010 *Phys. Rev.* B **81** 184425
[27] Ney A, Ollefs K, Ye S, Kammermeier T, Ney V, Kaspar T C, Chambers S A, Wilhelm F and Rogalev A 2008 *Phys. Rev. Lett.* **100** 157201
[28] Sati P, Deparis C, Morhain C, Schafer S and Stepanov A 2007 *Phys. Rev. Lett.* **98** 137204
[29] Bonanni A *et al* 2008 *Phys. Rev. Lett.* **101** 135502
[30] Bonanni A *et al* 2007 *Phys. Rev.* B **75** 125210
[31] Xu Q *et al* 2009 *J. Phys. D: Appl. Phys.* **42** 085001
[32] de Carvalho H B *et al* 2010 *J. Appl. Phys.* **108** 079906
[33] Bonanni A *et al* 2011 *Phys. Rev.* B **84** 035206
[34] Pereira L M C, Som T, Demeulemeester J, Van Bael M J, Temst K and Vantomme A 2011 *J. Phys.: Condens. Matter* **23** 346004
[35] Sarigiannidou E, Wilhelm F, Monroy E, Galera R M, Bellet-Amalric E, Rogalev A, Goulon J, Cibert J and Mariette H 2006 *Phys. Rev.* B **74** 041306
[36] Coey J M D, Venkatesan M and Fitzgerald C B 2005 *Nature Mater.* **4** 173
[37] Coey J M D, Stamenov P, Gunning R D, Venkatesan M and Paul K 2010 *New J. Phys.* **12** 053025
[38] Potzger K *et al* 2006 *Appl. Phys. Lett.* **88** 052508
[39] Wu P *et al* 2006 *Appl. Phys. Lett.* **89** 012508
[40] Song Y Y, Park K S, Son D V, Yu S C, Kang H J, Shin S W, Whang C N, Lee J H, Song J H and Lee K W 2007 *J. Korean Phys. Soc.* **50** 1706
[41] Kumar R, Singh A P, Thakur P, Chae K H, Choi W K, Angadi B, Kaushik S D and Patnaik S 2008 *J. Phys. D: Appl. Phys.* **41** 155002
[42] Robinson M T 1989 *Phys. Rev.* B **40** 10717
[43] Chu W K, Mayer J W and Nicolet M A 1978 *Backscattering Spectrometry* (New York: Academic)
[44] Hofsäss H and Lindner G 1991 *Phys. Rep.* **201** 121
[45] Hofsäss H, Wahl U and Jahn S G 1994 *Hyperfine Interact.* **84** 27
[46] Hofsäss H 1996 *Hyperfine Interact.* **97** 247
[47] Wahl U 2000 *Hyperfine Interact.* **129** 349
[48] Rita E, Wahl U, Correia J G, Alves E and Soares J C 2004 *Appl. Phys. Lett.* **85** 4899–901
[49] Pereira L M C, Wahl U, Decoster S, Correia J G, Amorim L M, da Silva M R, Araujo J P and Vantomme A 2011 *Phys. Rev.* B **84** 125204
[50] Wahl U, Rita E, Correia J G, Alves E and Soares J G 2004 *Phys. Rev.* B **69** 012102
[51] Fedoseyev V N *et al* 1997 *Nucl. Instrum. Methods Phys. Res.* B **126** 88
[52] Wahl U, Correia J G, Cardoso S, Marques J G, Vantomme A, Langouche G and ISOLDE Collaboration 1998 *Nucl. Instrum. Methods Phys. Res.* B **136** 744
[53] Agostinelli S *et al* 2003 *Nucl. Instrum. Methods Phys. Res.* A **506** 250
[54] Allison J *et al* 2006 *IEEE Trans. Nucl. Sci.* **53** 270
[55] Kucheyev S O, Williams J S, Jagadish C, Zou J, Evans C, Nelson A J and Hamza A V 2003 *Phys. Rev.* B **67** 094115
[56] Ambacher O 1998 *J. Phys. D: Appl. Phys.* **31** 2653
[57] Wahl U, Rita E, Correia J G, Alves E, Araujo J P and ISOLDE Collaboration 2003 *Appl. Phys. Lett.* **82** 1173

[58] Weyer G, Gunnlaugsson H P, Mantovan R, Fanciulli M, Naidoo D, Bharuth-Ram K and Agne T 2007 *J. Appl. Phys.* **102** 113915
[59] Gunnlaugsson H P *et al* 2010 *Appl. Phys. Lett.* **97** 142501
[60] Molholt T E *et al* 2009 *Physica* B **404** 4820
[61] Azamat D V and Fanciulli M 2007 *Physica* B **401** 382
[62] Khalid M, Setzer A, Ziese M, Esquinazi P, Spemann D, Poeppl A and Goering E 2010 *Phys. Rev.* B **81** 214414
[63] Ney A, Harris J S Jr and Parkin S S P 2006 *J. Phys.: Condens. Matter* **18** 4397
[64] Maeda K, Sato M, Niikura I and Fukuda T 2005 *Semicond. Sci. Technol.* **20** S49
[65] Heitz R, Hoffmann A and Broser I 1992 *Phys. Rev.* B **45** 8977
[66] Chikoidze E, von Bardeleben H J, Dumont Y, Galtier P and Cantin J L 2005 *J. Appl. Phys.* **97** 10D316
[67] Heitz R, Thurian P, Loa I, Eckey L, Hoffmann A, Broser I, Pressel K, Meyer B K and Mokhov E N 1995 *Appl. Phys. Lett.* **67** 2822
[68] Marcet S, Ferrand D, Halley D, Kuroda S, Mariette H, Gheeraert E, Teran F J, Sadowski M L, Galera R M and Cibert J 2006 *Phys. Rev.* B **74** 125201
[69] Behringer R E 1958 *J. Chem. Phys.* **29** 537
[70] Kittel C 2004 *Introduction to Solid State Physics* 8th edn (New York: Wiley)
[71] Dionne G F 2007 *J. Appl. Phys.* **101** 09C509
[72] Dionne G F and Kim H-S 2008 *J. Appl. Phys.* **103** 07B333
[73] Bi L, Kim H-S, Dionne G F and Ross C A 2010 *New J. Phys.* **12** 043044
[74] Jiang P, Bi L, Kim D H, Dionne G F and Ross C A 2011 *Appl. Phys. Lett.* **98** 231909
[75] Kim D H, Bi L, Jiang P, Dionne G F and Ross C A 2011 *Phys. Rev.* B **84** 014416
[76] Kim H-S, Bi L, Kim D H, Yang D-J, Choi Y J, Lee J W, Kang J K, Park Y C, Dionne G F and Ross C A 2011 *J. Mater. Chem.* **21** 10364–9
[77] Goodenough J B 1964 *J. Phys. Chem. Solids* **25** 151